Award Number: W81XWH-09-1-0299

TITLE: Photoacoustic Imaging of Epilepsy

PRINCIPAL INVESTIGATOR: Huabei Jiang, PhD

CONTRACTING ORGANIZATION: University of Florida
Gainesville, FL 32611

REPORT DATE: April 2010

TYPE OF REPORT: Annual

PREPARED FOR: U.S. Army Medical Research and Materiel Command
Fort Detrick, Maryland 21702-5012

REPORT DOCUMENTATION PAGE

Form Approved
OMB No. 0704-0188

1. REPORT DATE *(DD-MM-YYYY)*	**2. REPORT TYPE**	**3. DATES COVERED** *(From - To)*
04-30-2010	Annual	01 APR 2009 - 31 MAR 2010

4. TITLE AND SUBTITLE

Photoacoustic Imaging of Epilepsy

5a. CONTRACT NUMBER
W81XWH-09-1-0299

5b. GRANT NUMBER

5c. PROGRAM ELEMENT NUMBER

6. AUTHOR(S)

Huabei Jiang, PhD

Email: hjiang@bme.ufl.edu

5d. PROJECT NUMBER

5e. TASK NUMBER

5f. WORK UNIT NUMBER

7. PERFORMING ORGANIZATION NAME(S) AND ADDRESS(ES)

University of Florida
Biomedical Sciences Building
Gainesville, FL 32611

8. PERFORMING ORGANIZATION REPORT NUMBER

9. SPONSORING / MONITORING AGENCY NAME(S) AND ADDRESS(ES)

U.S. Army Medical Research
and Materiel Command
Fort Detrick, Maryland

10. SPONSOR/MONITOR'S ACRONYM(S)

11. SPONSOR/MONITOR'S REPORT NUMBER(S)

12. DISTRIBUTION / AVAILABILITY STATEMENT

Approved for public release; distribution unlimited

13. SUPPLEMENTARY NOTES

Photoacoustic imaging, photoacoustic tomography, epilepsy, seizure

14. ABSTRACT

This research is aimed at developing a new imaging approach, called "Photoacoustic tomography (PAT)", for non-invasively tracking dynamical changes during seizure occurrence. The project will develop imaging hardware and software, and conduct phantom/in vivo experiments to achieve the proposed goals. During the first year of this project, we have completed the design of the proposed array based PAT system based on the extensive modeling and testing of the key components needed for the system. We have also implemented a number of novel schemes that can enhance our current reconstruction software. We have conducted phantom experiments that confirmed our software enhancement.

15. SUBJECT TERMS

None provided.

16. SECURITY CLASSIFICATION OF:			**17. LIMITATION OF ABSTRACT**	**18. NUMBER OF PAGES**	**19a. NAME OF RESPONSIBLE PERSON**
a. REPORT	**b. ABSTRACT**	**c. THIS PAGE**			USAMRMC
U	U	U	UU	17	**19b. TELEPHONE NUMBER** *(include area code)*

Table of Contents

Introduction

Approximately 2.5 million Americans live with epilepsy and epilepsy-related deficits today, more than disabled by Parkinson disease or brain tumors. The impact of epilepsy in the US is significant with a total cost to the nation for seizures and epilepsy of approximately $12.5 billion. Epilepsy consists of more than 40 clinical syndromes affecting 40 million people worldwide. Approximately 25 percent of individuals receiving antiepileptic medication have inadequate seizure control; however, 80% individuals with medication resistant epilepsy might be cured through surgery if one were able to precisely localize the seizure focus. The proposed research will significantly advance our ability to localize such foci, and thereby offer curative epilepsy surgery for this devastating disease. Photoacoustic tomography (PAT) uniquely combines the high contrast advantage of optical imaging and the high resolution advantage of ultrasound imaging in a single modality. In addition to high resolution structural information, the proposed PAT is also able to provide functional information that are strongly correlated with regional or focal seizure activity, including blood volume and blood oxygenation because of the high sensitivity of optical contrast to oxyhemoglobin and deoxyhemoglobin concentrations. The hypothesis of the proposed research is that PAT offers the possibility to non-invasively track dynamical changes during seizure occurrence. The overall goal of this research is to advance a finite element based photoacoustic tomography method for epilepsy imaging, using both laboratory and in vivo experiments. Specifically, in this project we propose**:** (1) To design, construct and test a transducer array system for both 2D and 3D PAT imaging; (2) To advance reconstruction algorithms and associated image enhancement schemes for quantitative PAT; (3) To evaluate and optimize the integrated functioning of the hardware and software components of the transducer array-based system, using simulation and phantom experiments; (4) To test and validate the PAT system using a well established animal model of temporal lobe epilepsy.

Body

This report describes work accomplished in Year 1 (Months 0-12) of the project. As outlined in the approved Statement of Work (SOW), the tasks during this period of time include: **Task 1 (**Months 0-24): Purchase and calibrate Ti:Sapphire tunable laser; design and test PVDF transducers; design and test data acquisition subsystem; assemble the entire photoacoustic tomography (PAT) system; **Task 3 (**Months 0-24): Implement reconstruction codes and associated enhancing schemes including dynamic dual meshing, total variation, advanced regularization techniques, adaptive meshing, initial parameter optimization and reconstruction of absolute optical absorption coefficient for quantitative high resolution functional PAT.

The sections below consist of (1) hardware development and (2) software development that reflect the tasks associated with the SOW during Months 0-12.

1. Hardware Development (Task 1)

We have completed the design of the proposed array based PAT system based on the extensive modeling and testing of the key components needed for the proposed system using the existing single transducer scanning system. Purchases of all these components were already out, and we should be in a position to test each of the received components in next 2-3 months and ready to assemble the entire system during the summer. We are confident that we will be able to build an operational PAT system by the end of this year.

Here we detail our designing work for an array based PAT system which is schematically shown in Fig. 1a.

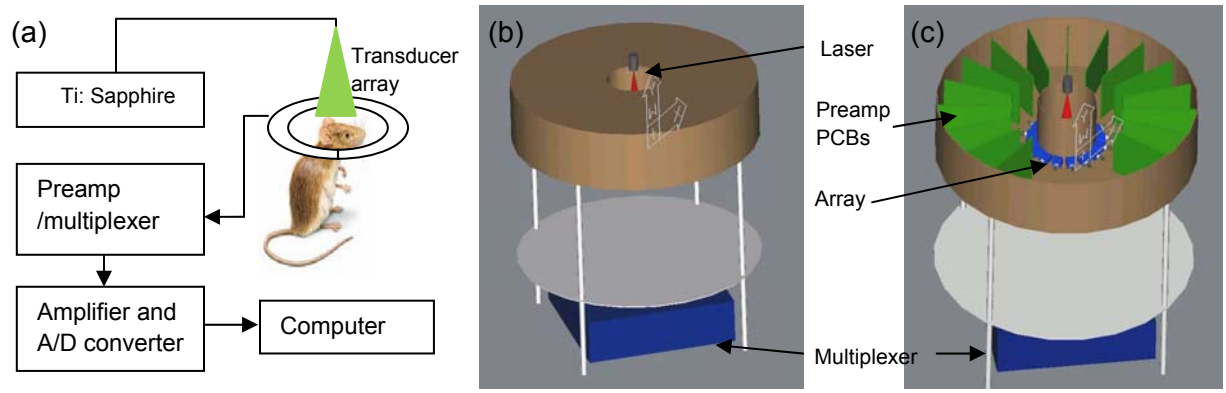

Fig. 1 (a) Schematic of the PAT system. (b) and (c): 3D display of the system/measurement chamber with (b) and without (c) the top covered.

1.1 Excitation light source

As proposed, a tunable Ti:Sapphire laser (690-900nm, 8-25ns pulse width, 120mJ between 760 and 800nm) is already in place that will be used as the light source.

1.2 Transducer array

Originally we proposed to customize a PVDF-based ring-type phase array with three rows of transducer elements. However, our recent study showed that the sensitivity of PVDF-based array is not good enough to guarantee high quality data collection especially when the working wavelength moves to near-infrared (NIR) (i.e., 690-900nm). So we decided considering to employ a phased array made of piezocomposite materials instead of PVDF for our PAT system. The cost of piezocomposite ring-type phased array (≥ $70,000), is much higher than a PVDF-based array. In order to reduce the cost for a phased transducer array, we have conducted numerical modeling and phantom experiments to see if we can use a flat 1.5D phased array to obtain imaging quality that is comparable to a ring-type phased array.

In the numerical simulations, a finite element code in time domain was used to generate the ultrasound signals at all detector locations and the delay-and-sum algorithm was used to reconstruct the photoacoustic images. Here the images obtained from a ring-type array and an array formed by 8-piece flat elements are compared. Two kinds of targets, circles and crosses, were embedded in a background medium. Fig. 2 shows the exact (a & d) and reconstructed photoacoustic images (b, c, e, & f) when each element was treated as an ideal point transducer that can receive signals coming from all angles. We see that the reconstructed images from the two types of arrays are almost identical.

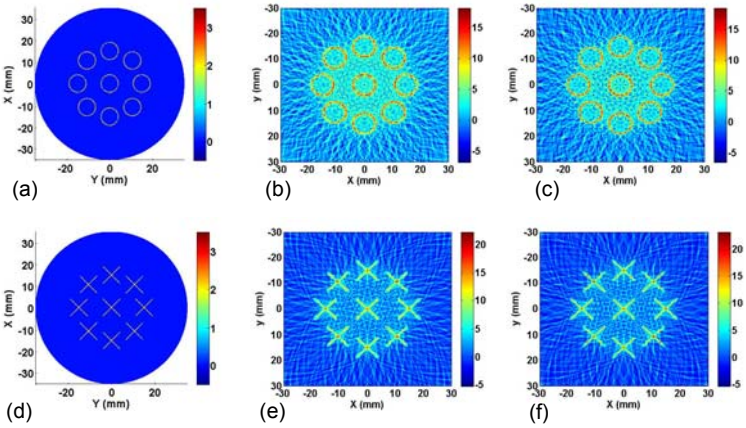

Fig. 2. Simulation results without applying transducer directivity. (a) & (d): the exact images. (b) & (e): reconstructed images based on a ring-type array. (c) & (f): reconstructed images an 8-piece flat element-based array.

In a real situation, each transducer element has directivity, meaning that it can only collect ultrasound signal from a limited angle, depending on its size and central frequency. Fig. 3 shows the typical 2D fields from a 5MHz transducer with 2mm in diameter and a 4MHz transducer with 1.5mm in diameter. Generally, a transducer with smaller size and lower central frequency has bigger receiving angle, but lower sensitivity and poorer spatial resolution. Considering all the trade-offs among spatial resolution, sensitivity and receiving angle, transducer elements with a central frequency of 4MHz and a dimension of 1.5mmx2.0mm will be used in our application. Fig. 4 gives the field coverage of the ring-type array and 8-piece flat array.

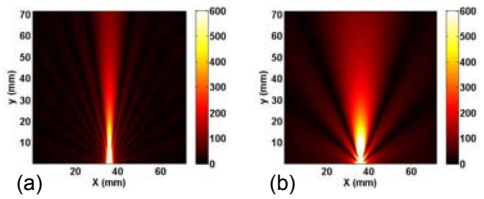

Fig. 3. Calculated 2D fields from (a) 5MHz Φ2mm and (b) 4MHz Φ1.0mm transducer element.

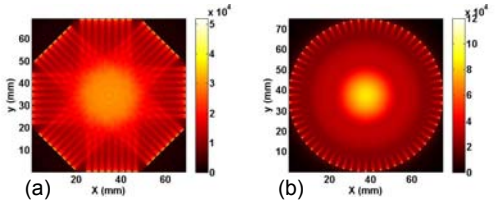

Fig. 4. 2D field coverage of (a) the ring-type array and (b) the 8-piece flat array. The dimension of the transducer elements is 1.5x2.0mm and the central frequency is 4MHz.

When the directivity of each transducer element is considered in the numerical simulations, the results show that the 8-piece flat array can still provide satisfactory image quality (Fig. 5).

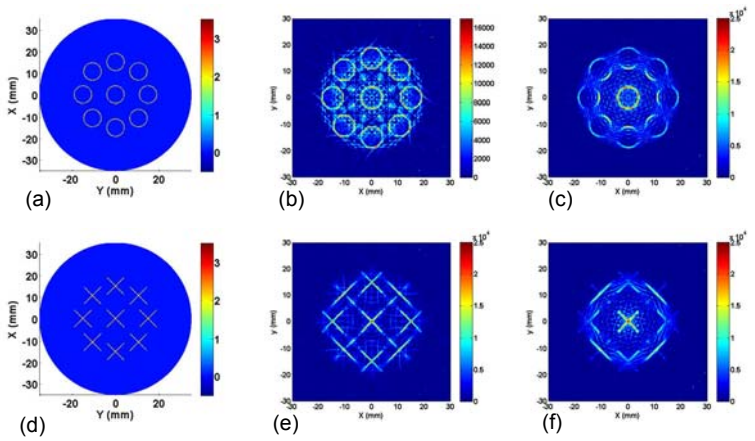

Fig. 5. Simulation results with directivity considered. (a) & (d): the exact images. (b) & (e): reconstructed images based on a single ring-type array. (c) & (f) reconstructed images based on 8-piece flat array.

We have conducted phantom experiments to confirm the simulation findings. In the experiments, multiple hairs were embedded in a gel phantom background (see a photograph shown in Fig. 6a). A single transducer with 2mm in diameter, driven by a motorized rotator and a linear stage was used to collect the ultrasound signals along a circular path (simulating a ring-type array) and along an arc-straight line path (simulating an 8-, 16-, and 32-piece flat array). The experimental images are shown in Fig. 6 (b-e). Taking a close look at the recovered images, we found that some structures were missed in the image from a simulated 8-piece flat array. We realized that this was due to the missing of ultrasound signals from some directions for this array configuration. We note that the image from a simulated 16-piece flat array gives almost the same quality as the simulated ring-type array. Based on these phantom experiments, we decided that a16-piece flat array (4x3 elements each piece) will be used for our PAT system. The cost for this array is reduced by ≥ $12,000 compared to a ring-type array.

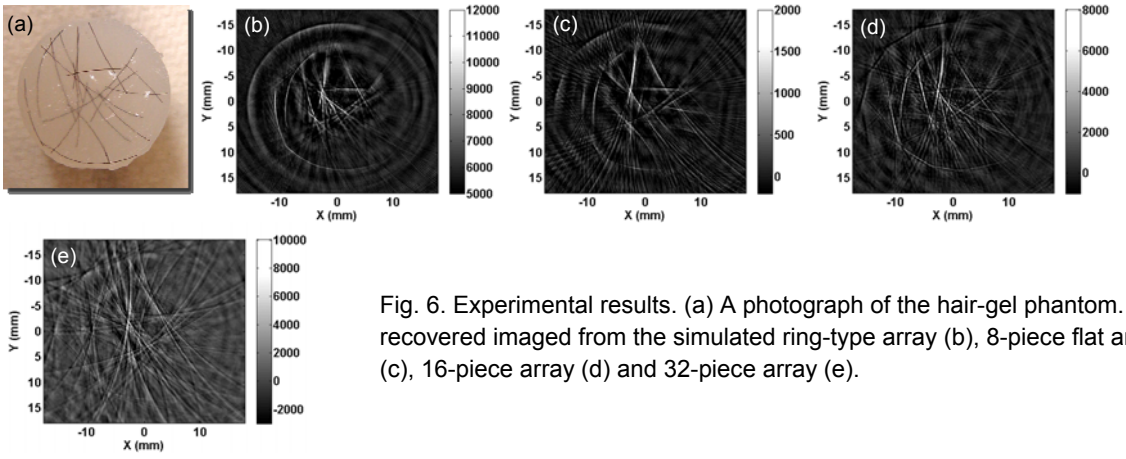

Fig. 6. Experimental results. (a) A photograph of the hair-gel phantom. The recovered imaged from the simulated ring-type array (b), 8-piece flat array (c), 16-piece array (d) and 32-piece array (e).

The 16-piece flat transducer arrays will be arranged along a circular path with a radius of 41mm. We asked quotations for such a flat array from three companies including GE (Lewistown, PA), Olympus-IMS (Waltham, MA), and Imasonic SAS (l'Ognon, France), and we decided to buy from Imasonic SAS as it is the most cost-effective. In this array, each piece comes with 3 (row) x 4 (column) elements, which are directly cabled, and each of them acts as an independent detecting channel, making a total of 192 channels on three rows for the whole array subsystem. The central frequency of the elements is 4MHz with 60% bandwidth. The dimension of each element is 2.0 x 1.5mm. Fig. 7 shows the structure of the detection unit as well as the distribution of the elements in each transducer array.

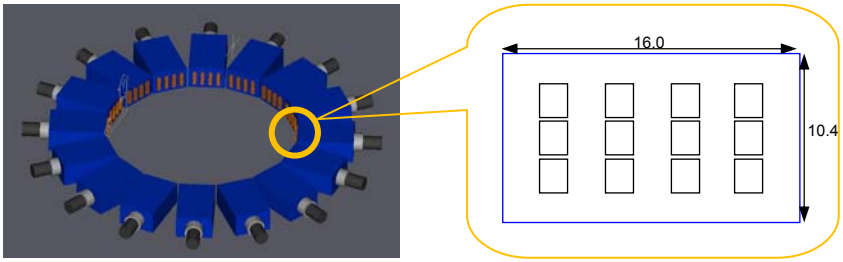

Fig. 7. The arrangement of 16-piece flat array. The insert shows the distribution of elements in one array.

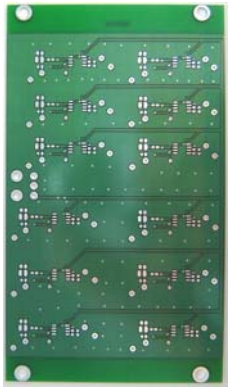

Fig. 8. PCB under testing for 12-channel preamplifiers.

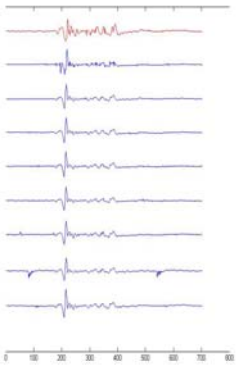

Fig. 9. Testing result of ultrasound signal: red, from the Olympus 5058PR ; blue: from the PCIAD850 1~8 channel, respectively.

1.3 Data acquisition (Preamplifiers, multiplexer and A/D board)

The originally proposed data acquisition system, DiPhAS by Fraunhofer Institute for Biomedical Engineering (St. Ingbert, Germany), contains preamplifiers, signal processing and multi-channel A/D boards in one package and provides quality needed for the proposed study. However, the price of this system is increased significantly since early 2009 (before the start of this project), and the approved budget of the project does not allow us to buy this system. Since there is no commercial one-package data acquisition affordable to us in the current market, we decided to do the following to resolve the issue: purchase the A/D boards and build preamplifiers ourselves.

We have a total of 192 signal channels (corresponding to 192 transducer elements from the array). Each channel will need a preamplifier. The design of preamplifier is based on ultralow distortion, ultralow noise and high speed AD8099 operational amplifier from Analog Device, which can provide 26dB gain. Bandwidth filters have been added to the preamplifier circuits to further decrease the noise level. Fig. 8 is the designed 12-channel PCB (printed circuit board). A total of sixteen 12-channel PCBs will be used and placed right beside the 16-piece flat transducer array, see Fig. 1c.

Ideally we would need a 192-channel A/D boards, but the cost is far beyond the approved budget for equipment. Instead we just can afford a 64-channel A/D boards (US Ultratek Concord, CA). The data acquisition from all 192 channels is realized via an integration of the 64-channel boards and a multiplexer. The 64-channel A/D boards, PCIAD850/PCIAD1650, can provide 50MHz sampling rate for all channels at a resolution up to 10bit. The on-board gain can be adjusted separated for each channel from -12dB to 84dB. A demo board from this manufacturer has been tested and has been compared to the 5058PR, a commercial single channel pulser/receiver from Olympus. The comparative measurements are shown in Fig. 9, indicating that the performance of these data acquisition boards is satisfactory for our project.

As indicated above, the ultrasound signals from the 192 channels will be selected and delivered to 64 parallel data acquisition channels through a multiplexer placed under the imaging interface as shown in Fig. 1b-c. The multiplexer will be purchased from Cytec Corp. (Penfield, NY). We are also making effort on another option by integrating multiplexer into the preamplifier PCBs. The advantages of this solution include the more compactness of the system, lower noise and lower cost.

The computer, which is used for system control and data storage, will be an industrial 4U PC with a dual-core processor and at least 8 PCI slots. We have a solution from Acnodes Corporation (Walnut, CA). A LabVIEW program will be used to control the whole system.

2. Software Development (Task 3)

In Task 3, we will implement 6 image enhancement schemes. In Year 1, we have chosen to complete the implementation of 3 schemes including total variation (TV), advanced regularization techniques, and adaptive meshing. We will implement the remaining 3 schemes in Year 2.

2.1 Total variation minimization

The concept of TV was originally conceived as a way of restoring/enhancing images (e.g., denoising, deblurring etc.). Conventional PAT reconstruction algorithms are based on a nonlinear least squares criterion which stands on the statistical argument that the least squares estimation is the best over an entire ensemble of all possible pictures. TV, on the other hand, measures the oscillations of a given objective function and does not unduly punish discontinuities. Hence, we have hypothesized that a hybrid of these two minimization schemes should be able to provide higher quality image reconstruction. We have successfully implemented the TV scheme into the existing reconstruction codes (see the Appendix for mathematical detail). We have evaluated the TV scheme using experimental data. For

comparative purposes, reconstructions without the total-variation-minimization enhancement are also presented.

Three phantom experiments were conducted. In the first two experiments, we embedded one or two objects with a size ranging from 3 to 0.5 mm in a 50 mm-diameter solid cylindrical phantom. The phantom materials used consisted of Intralipid as scatterer and India ink as absorber with Agar powder (1-2%) for solidifying the Intralipid and India ink solution. The absorption coefficient of the background phantom was 0.01 mm^{-1}, while the absorption coefficient of the target(s) was 0.03 mm^{-1}. In the last experiment, we used a single-target-containing phantom, aiming to test the capability of detecting target having low optical contrasts relative to the background phantom. In this case, the target had an absorption coefficient of 0.015 mm^{-1}. The reduced scattering coefficients of the background phantom and targets were 1.0 and 3.0 mm^{-1} for the first two experiments, and 1.0 and 2.0 mm^{-1} for the last experiment. In these experiments, a total of 120 receivers were equally distributed along the surface of the circular background region.

Figure 10 shows the reconstructed photoacoustic images for all the three experimental cases, while Figure 11 presents quantitative absorption profiles along transacts through one target for the images shown in Fig. 10. We see that considerably enhanced images are achieved with the total-variation minimization, especially when the target is tiny (case 2), or the contrast level between the target and the background is low (case 3).

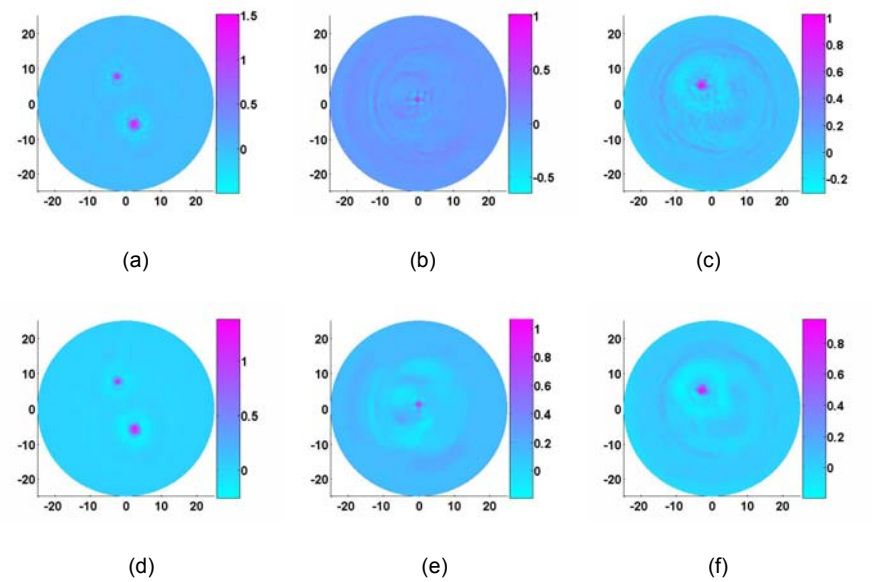

Fig.10 Reconstructed absorbed energy density images. (a) case 1 without TV minimization, (b) case 2 without TV minimization, (c) case 3 without TV minimization, (d) case 1 with TV minimization, (e) case 2 with TV minimization, (f) case 3 with TV minimization.

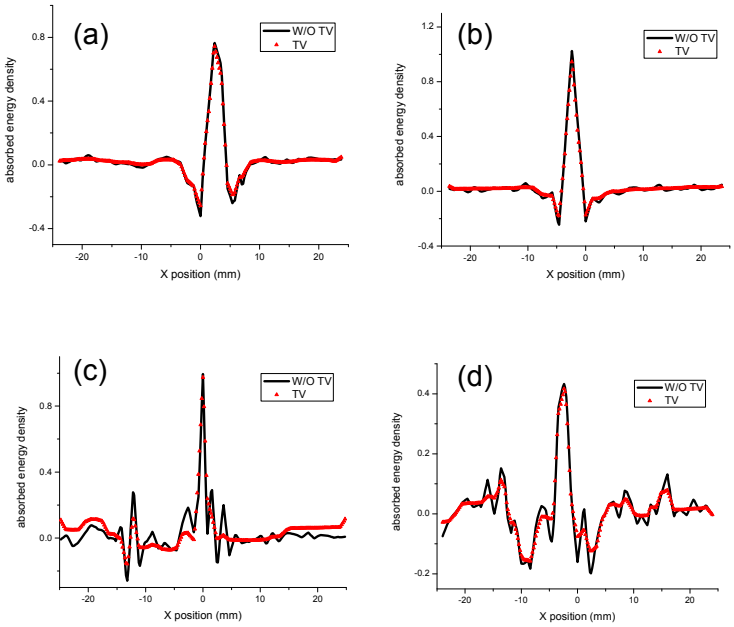

Fig. 11 Recovered absorbed energy density profiles along (a) y=-7.0mm for case 1 (3mm diameter target), (b) y=8.0mm for case 1 (2mm diameter target), (c) y=1.0mm for case 2, (d) y=6.5mm for case 3.

2.2 Advanced regularization techniques

Image reconstruction is typically an ill-posed problem. That is, its solution procedures can become singular or nearly-singular such that small errors in the measured data are magnified significantly in the resulting image. Regularization techniques are practical methods which have proven to be able to combat the ill-posed problems associated with noisy data. We have implemented a prototype hybrid technique which synthesizes standard Marquardt and Tikhonov regularization schemes in the existing reconstruction codes. As proposed, we have attempted to further evaluate and optimize this method in Year 1. Fig. 12 shows a set of typical reconstructions for the optimization study where the regularization parameter, λ, is varied from 0.6×10^{2} to 0.6×10^{-6} for a test case having three targets embedded in a circular background medium. We note that these images are similar qualitatively; however, quantitatively in terms of the recovered optical absorption (see the color bar on the right), $\lambda=0.6\times10^{-1}$(d) and $\lambda=0.6\times10^{-2}$ (e) give the best results.

We have also implemented the weighted least squares criterion in our reconstruction algorithms. Fig. 13 gives the reconstructed images from a typical test. We see that both images are almost identical, but as expected, the reconstruction with the weighted least squares criterion converged 50% faster than that without such criterion.

We have implemented a spatial low pass filter in our algorithms, which acts on the photoacoustic property distribution during the iterative reconstruction process. Fig. 14 shows the images from the three-target example. We note that this filtering is useful in reducing the noise effect in the background and improved the quantitative nature of the recovered photoacoustic property (see the color bar on the right).

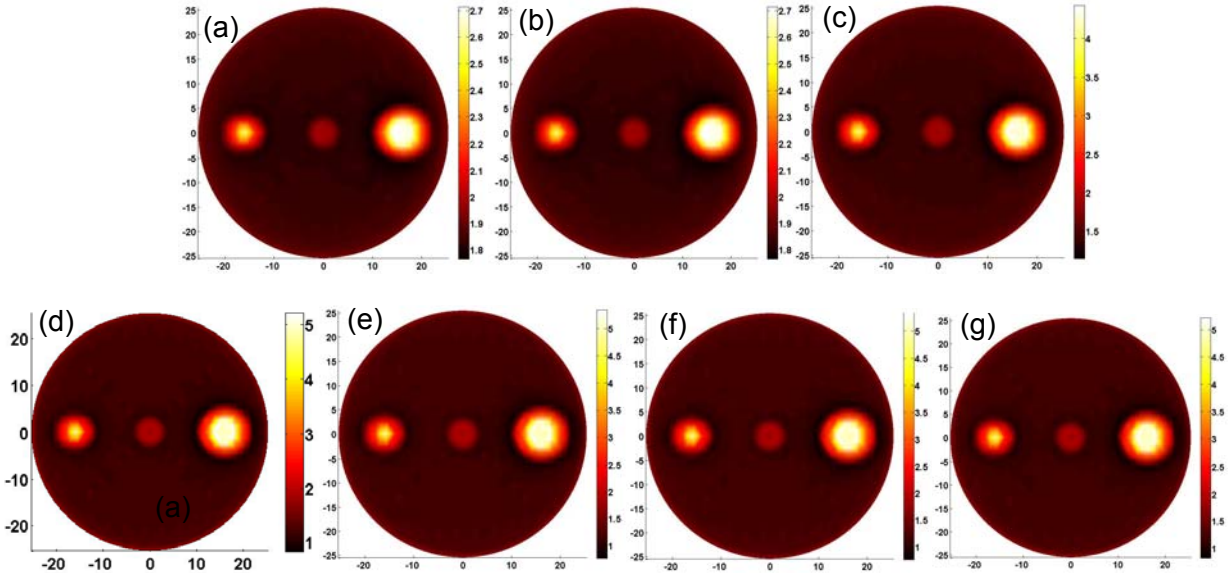

Fig. 12. Reconstructed photoacoustic images. Left target: 5mm in diameter and 4:1 contrast; middle target: 3 mm in diameter and 3:1 contrast; right target: 8 mm in diameter and 5:1 contrast. (a): $\lambda=0.6\times10^{2}$. (b): $\lambda=0.6\times10^{1}$. (c): $\lambda=0.6$. (d): $\lambda=0.6\times10^{-1}$. (e): $\lambda=0.6\times10^{-2}$. (f): $\lambda=0.6\times10^{-4}$. (g): $\lambda=0.6\times10^{-6}$.

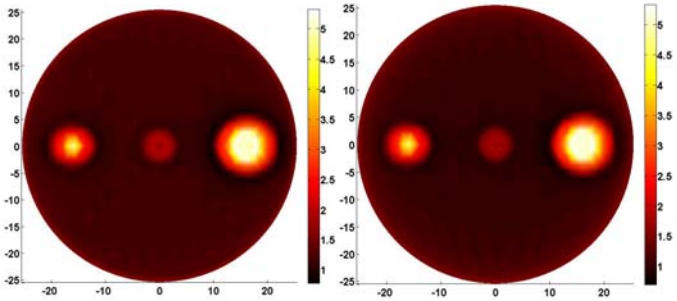

Fig. 13. Reconstructed photoacoustic images without (left) and with (right) the weighted least squares criterion.

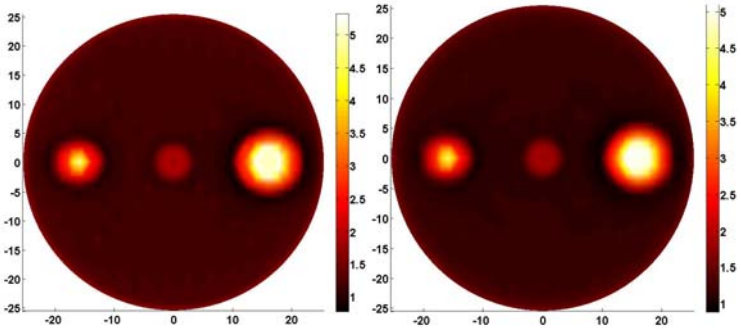

Fig. 14. Reconstructed images without (left) and with (right) spatial filtering.

2.3 Adaptive meshing

We have successfully implemented the adaptive meshing scheme in the reconstruction codes. In this scheme, we locally refine the property mesh in areas where the interelement property gradient exceeds a preset maximum value. At boundaries of heterogeneities one would expect

large gradients in the property distribution; hence this scheme will adaptively refine such areas. Reconstructed results from two representative cases are shown in Fig. 15 where the uniform and adaptive meshes used are also given. We see that the target is clearly better recovered with the adaptive mesh (d & f) in terms of its shape and size over that with the uniform mesh (c & e) for both cases. We also note that the background region for both cases is more smoothly recovered with the adaptive mesh compared to that with the uniform mesh.

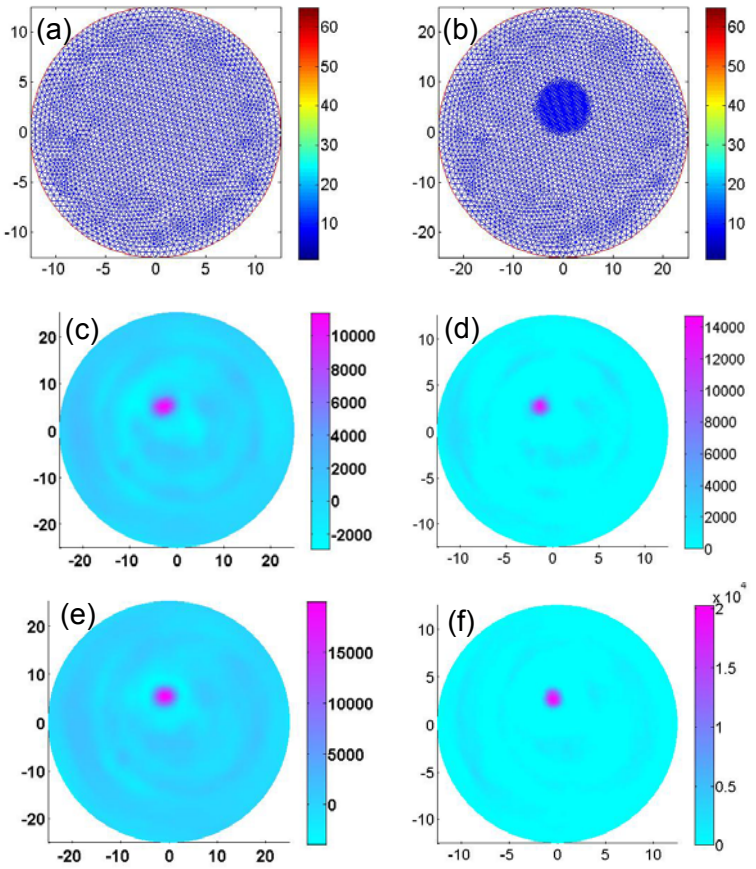

Fig. 15. Reconstructed photoacoustic images from experimental data. (a): the uniform finite element mesh used (2458 nodes). (b): the mesh locally adapted around the target region (3882 nodes). (c): the image for case 1 with uniform mesh. (d): the image for case 1 with adaptive mesh. (e): the image for case 2 with uniform mesh. (d): the image for case 2 with adaptive mesh. Case 1: a 2-mm-diameter target having 1.5:1 contrast. Case 2: a 2-mm-diameter target having 2:1 contrast.

Key Research Accomplishments

1. We have completed the design for an array based PAT system, which is the most important part of Task 1.
2. We have developed three novel schemes that can enhance our current reconstruction software.
3. We have conducted phantom experiments that confirmed our software enhancement.

Reportable Outcomes (see the Appendix to this Summary Report)

Conclusions

We have made a significant progress that has fulfilled the statement of work proposed for Year 1 of this project. Given the successful first year, we will be able to fulfill or exceed the work statement for Year 2.

Appendix

L. Yao and H. Jiang, Enhanced time-domain photoacoustic tomography through total-variation minimization, in Biomedical Optics 2010 Technical Digest (Optical Society of America, Miami, Florida, 2010).

Enhanced Time-domain Photoacoustic Tomography through Total-variation Minimization

Lei Yao and Huabei Jiang
Department of Biomedical Engineering, University of Florida, Gainesville, FL 32611
Email: hjiang@bme.ufl.edu

Abstract: A total-variation-minimization-based iterative algorithm is described in this paper that enhances the quality of reconstructed images with time-domain data over that obtained previously with a regularized least-squares approach.

OCIS codes: (110.6960) Tomography; (110.5120) Photoacoustic imaging

1. Introduction

Photoacoustic tomography (PAT) is an emerging non-invasive imaging technique that combines the merits of high optical contrast and high ultrasound resolution in a single modality [1-3]. In PAT, the Helmholtz-like photoacoustic (PA) wave equation has been commonly used as an accurate model for describing laser-induced acoustic wave propagation in tissue. While analytical reconstruction methods have been used for photoacoustic image reconstructions, finite element method (FEM) based method appears to be particularly powerful in this regard [4, 5]. In our previous work, extensive simulations and experiments with frequency-domain measurements have been conducted, and maps of the absorbed energy density in multicentimeter phantom geometries has been achieved with a Newton iterative algorithm used in conjunction with finite element methods [4-6]. Recently there has been considerable interest in time-domain schemes, since this algorithm shows its advantages when recovering absorbed energy density images, such as less background artifacts, more accurately recovered object size and contrast between the object and background [7]. Although encouraging successes with model-based image reconstruction have been reported, noise can be a significant limitation for these techniques. Our own experience in this regard has revealed that the quantitative quality of reconstruction is affected considerably when data with large noise level is used.

In this study, we propose the incorporation of a total-variation-minimization scheme into our time-domain PAT reconstruction algorithm to reduce the effects of noise and to enhance the quality of the reconstructed images. We demonstrate the new scheme using several tissue-like phantom experiments.

2. Total-Variation-Minimization Scheme

To describe our total-variation-minimization method, we first briefly introduce the time-domain photoacoustic reconstruction algorithm with the regularized Newton method we have used previously [4-7]. The time-domain photoacoustic wave equation in tissue can be described as follows

$$\nabla^2 p(\mathbf{r},t) - \frac{1}{v_0^2}\frac{\partial^2 p(\mathbf{r},t)}{\partial t^2} = -\frac{\Phi(\mathbf{r})\beta}{C_p}\frac{\partial J(t)}{\partial t}, \qquad (1)$$

where p is the pressure wave; v_0 is the speed of acoustic wave in the medium,; β is the thermal expansion coefficient; C_p is the specific heat; Φ is the absorbed energy density; $J(t)=\delta(t-t_0)$ is assumed in our study. To form an image from a presumably uniform initial guess of the absorbed energy density distribution we need a method of updating Φ from its starting value. This update is accomplished through the least-squares minimization of

$$F(p,\Phi)=\sum_{j=1}^{M}\left(p_j^0 - p_j^c\right)^2, \qquad (2)$$

where p_j^0 and p_j^c are observed and computed acoustic field data for $i=1,2,\cdots M$ boundary locations. Using a regularized Newton method, we obtained the following equation for updating Φ:

$$\left(\Im^T\Im+\lambda I\right)\Delta\chi=\Im^T\left(p^0-p^c\right), \qquad (3)$$

where $p^0 = \left(p_1^0, p_2^0, \cdots p_M^0\right)^T$, $p^c = \left(p_1^c, p_2^c, \cdots p_M^c\right)^T$, $\Delta\chi$ is the update vector for the absorbed optical energy density, $\Im$ is the Jacobian matrix formed by $\partial p/\partial\Phi$ at the boundary measurement sites; λ is the regularization parameter determined by combined Marquardt and Tikhonov regularization schemes, and **I** is the identity matrix.

We now incorporate the total variation of Φ as penalty term by defining a new functional [8-11]:

$$\widetilde{F}(p,\Phi) = F(p,\Phi) + L(\Phi), \quad (4)$$

where $L(\Phi) = \int\sqrt{\omega_\Phi^2\left|\nabla\Phi\right|^2 + \delta^2}\,dxdy$ is the penalty term, ω_Φ and δ are typically positive parameters that need to be determined numerically. The minimization of Eq. (4) proceeds in standard fashion by the differentiation of $\widetilde{F}$ with respect to each nodal parameter that constitutes the Φ distribution; simultaneously all these relations are set to zero. Then we find that the minimizers of Eq. (4) are iteratively found by solving the matrix system

$$\left(\Im^T\Im + R + \lambda I\right)\Delta\chi = \Im^T\left(p^0 - p^c\right) - V, \quad (6)$$

where *V* is formed by $\partial L/\partial\Phi$ and *R* is formed by $\partial V/\partial\Phi$. After Eq. (6) has been reached, our solution procedure (standard Gausssian elimination) and regularization parameter selection (Marquardt method) are identical to those used previously. Hence, it becomes clear that the only additions to our new algorithm result from the assembly of matrix *R* and the construction of column vector *V*.

3. Results

In this section the enhanced reconstruction algorithm with total-variation minimization is evaluated with some experiment data. For comparative purposes, reconstructions without the total-variation-minimization enhancement (i.e., those which use our previous regularized Newton method) are also presented.

The experimental setup used for collecting experimental data is a pulsed ND:YAG laser based single transducer (1MHz) scanning system, which was described in detail elsewhere [5]. Three phantom experiments were conducted. In the first two experiments, we embedded one or two objects with a size ranging from 3 to 0.5 mm in a 50 mm-diameter solid cylindrical phantom. The phantom materials used consisted of Intralipid as scatterer and India ink as absorber with Agar powder (1-2%) for solidifying the Intralipid and India ink solution. The absorption coefficient of the background phantom was 0.01 mm^{-1}, while the absorption coefficient of the target(s) was 0.03 mm^{-1}. In the last experiment, we used a single-target-containing phantom, aiming to test the capability of detecting target having low optical contrasts relative to the background phantom. In this case, the target had an absorption coefficient of 0.015 mm^{-1}. The reduced scattering coefficients of the background phantom and targets were 1.0 and 3.0 mm^{-1} for the first two experiments, and 1.0 and 2.0 mm^{-1} for the last experiment.

A total of 120 receivers were equally distributed along the surface of the circular background region. We chose $T = 3.0\times10^4\,ns$ as the time range and $\Delta t = 200ns$ as the time interval for the image reconstructions since longer time range and shorter time interval do not appear to provide better reconstruction results. We also implemented a dual meshing method for fast yet accurate inverse computation. The fine mesh used for the forward calculations consisted of 5977 nodes and 11 712 elements, while the coarse mesh used for the inverse calculations had 1525 nodes and 2928 elements. All the images obtained from regularized Newton method are the results of three iterations, while those obtained from the total-variation minimization are results of fifteen iterations. (We found that larger number of iteration changed the solutions only by less than 0.5%). Parallel code was used to perform these calculations and each iteration cost ~40 minutes on Beowulf clusters with 4 CPUs. For the cases presented, values of $\omega_\Phi = 1.0, \delta = 0.001$ for the first and third case, and $\omega_\Phi = 2.0, \delta = 0.001$ for the second case appear to provide excellent results.

Figure 1 shows the reconstructed absorption coefficient images for all the three experimental cases, while Figure 2 presents quantitative absorption coefficient profiles along transacts through one target for the images shown in Fig. 1. We see that considerably enhanced images are achieved with the total-variation minimization, especially when the target is tiny (case 2), or the contrast level between the target and the background is low (case 3).

BSuD6.pdf

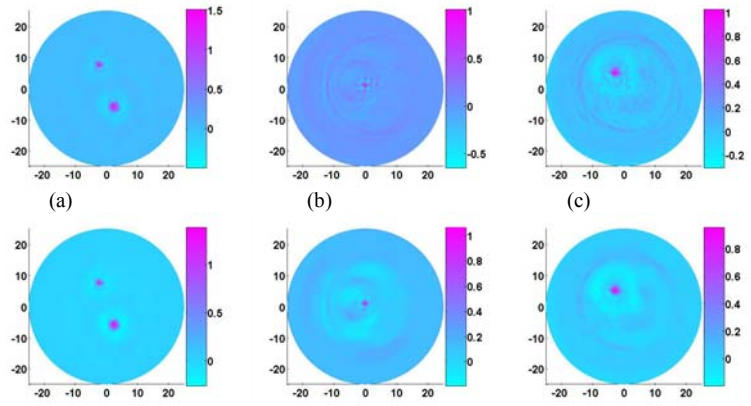

(a) (b) (c)

(d) (e) (f)

Fig.1 Reconstructed absorbed energy density images. (a) reconstruction of case 1 with no TV minimization, (b) reconstruction of case 2 with no TV minimization, (c) reconstruction of case 3 with no TV minimization, (d) reconstruction of case 1 with TV minimization, (e) reconstruction of case 2 with TV minimization, (f) reconstruction of case 3 with TV minimization.

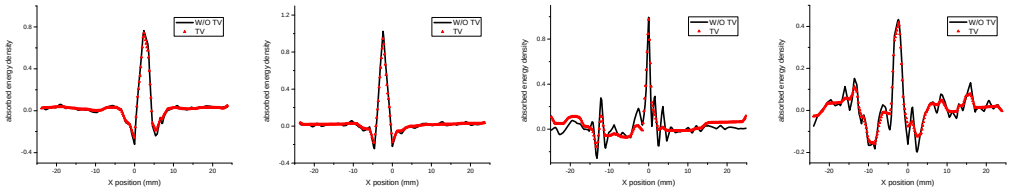

(a) (b) (c) (d)

Fig. 2 Recovered absorbed energy density profiles along (a) y=-7.0mm for case 1 (3mm diameter target), (b) y=8.0mm for case 1 (2mm diameter target), (c) y=1.0mm for case 2, (d) y=6.5mm for case 3.

In summary, we have demonstrated time-domain photoacoustic image reconstructions using an algorithm that is based on total-variation minimization. The results have shown that enhancements of the reconstruction images have been achieved when the new algorithm is compared with the regularized least-squares minimization. This new method may have largest impact on image recovery for cases having low contrast levels between the target and the background, or cases having tiny heterogeneities.

Acknowledgement

The research was support in part by the Department of Defense Congressionally Directed Medical Program.

References

[1] G. Paltauf, J. Viator, S. Prahl, and S. Jacques, "Iterative reconstruction algorithm for optoacoustic imaging," *J. Acoust. Soc. Am.* **112**, 1536-1544 (2002).
[2] S. J. Norton and T. Vo-Dinh, "Optoacoustic diffraction tomography: analysis of algorithms," *J. Opt. Soc. Am.* **A 20**, 1859-1866 (2003).
[3] A. A. Oraevsky, A. A. Karabutov, S. V. Solomatin, E. V. Savateeva, V. A. Andreev, Z. Gatalica, H. Singh, R. D. Fleming, "Laser optoacoustic imaging of breast cancer in vivo," in *Biomedical Optoacoustics II*, ed A. A. Oraevsky, Proc. SPIE **4256**, 6-15 (2001).
[4] Z. Yuan and H. Jiang, "Quantitative photoacoustic tomography: Recovery of optical absorption coefficient maps of heterogeneous media," *Appl. Phys. Lett.* **88**, 231101 (2006).
[5] L. Yin, Q. Wang, Q. Zhang, and H. Jiang, "Tomographic imaging of absolute optical absorption coefficient in turbid media using combined photoacoustic and diffusing light measurements," *Opt. Lett.* **32**, 2556-2558 (2007).
[6] H. Jiang, Z. Yuan, and X. Gu, "Spatially varying optical and acoustic property reconstruction using finite-element-based photoacoustic tomography," *J. Opt. Soc. Am.* **A 23**, 878-888 (2006).
[7] L. Yao and H. Jiang, "Finite-element-based photoacoustic tomography in time-domain", *J. Opt. A: Pure Appl. Opt.* **11**, 085301 (2009).
[8] K. D. Paulsen and H. Jiang, "Enhanced frequency-domain optical image reconstruction in tissues through total-variation minimization", App. Opt., 35, 3447-3458 (1996).
[9] P. M. van den Berg and R. E. Kleinmann, "A total variation enhanced modified gradient algorithm for profile reconstruction," Inverse Probl. **11**, L5-L10 (1995).
[10] C. R. vogel and M. E. Oman, "Iterative methods for total variation denoising," SIAM J. Sci. Comput. **17**, 227-238 (1996).
[11] D. C. Dobson and F. Santosa, "Recovery of blocky images from noisy and blurred data," SIAM J. Appl. Math. **56**, 1181-1198 (1996).